

---

Title	Challenges and applications to operando and in situ TEM imaging and spectroscopic capabilities in a cryogenic temperature range
Author(s)	Elizaveta Tyukalova, Joseph Vas, Reinis Ignatans, Aaron David Mueller, Rohit Medwal, Masaaki Imamura, Hironori Asada, Yasuhiro Fukuma, Rajdeep Singh Rawat, Vasiliki Tileli and Martial Duchamp

---

Copyright © 2021 ACS Publications

This is the author's accepted manuscript (post-print) and the final, definitive version of this paper has been published in *Accounts of Chemical Research*, Volume 54, Issue 16, 3125–3135. <https://doi.org/10.1021/acs.accounts.1c00078> by ACS publishing. All rights reserved.

# Challenges and applications to *operando* and *in situ* TEM imaging and spectroscopic capabilities in a cryogenic temperature range

Elizaveta Tyukalova<sup>1#</sup>, Joseph Vas<sup>2#</sup>, Reinis Ignatans<sup>3</sup>, Aaron David Mueller<sup>1</sup>, Rohit Medwal<sup>2</sup>, Masaaki Imamura<sup>4</sup>, Hironori Asada<sup>5</sup>, Yasuhiro Fukuma<sup>6, 7</sup>, Rajdeep Singh Rawat<sup>2</sup>, Vasiliki Tileli<sup>3</sup>, Martial Duchamp<sup>1\*</sup>

<sup>1</sup>Laboratory for *in situ* and *operando* Electron Nanoscopy, School of Material Science and Engineering, Nanyang Technological University, Singapore 637616 Singapore

<sup>2</sup>Natural Sciences and Science Education, National Institute of Education, Nanyang Technological University, Singapore 637616 Singapore

<sup>3</sup>Institute of Materials, École Polytechnique Fédérale de Lausanne, CH-1015 Lausanne, Switzerland

<sup>4</sup>Department of Electrical Engineering, Fukuoka Institute of Technology, Fukuoka 811-0295, Japan

<sup>5</sup>Graduate School of Sciences and Technology for Innovation, Yamaguchi University, Ube 755-8611, Japan

<sup>6</sup>Department of Physics and Information Technology, Kyushu Institute of Technology, Iizuka 820-8502, Japan

<sup>7</sup>Research Center for Neuromorphic AI Hardwares, Kyushu Institute of Technology, Kitakyushu 808-0196, Japan

# Equal contribution authors

\* Corresponding author

## CONSPECTUS

In this account, we describe challenges and promising applications of transmission electron microscopy (TEM) imaging and spectroscopy at cryogenic temperatures. Our work focuses on two areas of applications, **to delay electron beam-induced degradation** and **to follow low temperature phenomena in a continuous and variable temperature range**. For the former, we present a study of  $\text{LiMn}_{1.5}\text{Ni}_{0.5}\text{O}_4$  lithium-ion battery cathode material that undergoes electron beam-induced degradation when studied at room temperature by TEM. Cryogenic imaging reveals the true structure of  $\text{LiMn}_{1.5}\text{Ni}_{0.5}\text{O}_4$  nanoparticles in its discharged state. Improved stability under electron beam irradiation was confirmed by following the evolution of the O K-edge fine structure by electron energy-loss spectroscopy. Our results demonstrate that the effect of radiation damage on discharged  $\text{LiMn}_{1.5}\text{Ni}_{0.5}\text{O}_4$  was previously underestimated and that atomic resolution imaging at cryogenic temperature has a potential to be generalized to most of the Li-based materials and beyond. For the latter, we present two studies in the imaging of low temperature phenomena at local scale, namely, the evolution of ferroelectric and ferromagnetic domains walls, in  $\text{BaTiO}_3$  and  $\text{Y}_3\text{Fe}_5\text{O}_{12}$  systems, respectively, in a continuous and variable temperature range. Continuous imaging of phase transition in  $\text{BaTiO}_3$ , a prototypical ferroelectric system, from low temperature orthorhombic phase continuously up to centrosymmetric high temperature phase is shown to be possible inside a TEM. Similarly, the propagation of domain walls in  $\text{Y}_3\text{Fe}_5\text{O}_{12}$ , a magnetic insulator, is studied from  $\sim 120$  K to  $\sim 400$  K and combined with application of magnetic field and electrical current pulses to mimic the *operando* conditions as in domains wall memory and logic devices for information technology. Such studies are promising to study the pinning of the ferroelectric and magnetic domains versus temperature, spin polarized current and externally applied magnetic field to better manipulate the domain walls. The capability of combining *operando* TEM stimuli such as current, voltage, and/or magnetic field with *in situ* TEM imaging in a continuous cryogenic temperature range will allow the uncovering of fundamental phenomena at nanometer scale. These studies were made possible using a MEMS-based TEM holder that allowed an electron transparent sample to be transferred and electrically contacted on a MEMS chip. The six-contact double-tilt holder allows alignment of the specimen into its zone-axis while simultaneously using four electrical contacts to regulate the temperature and two contacts for applying the electrical stimuli, i.e., *operando* TEM imaging. This account leads to the demonstration of (i) high-resolution imaging and spectroscopy of nanoparticles oriented in the desired [110] zone-axis direction at cryogenic temperatures to mitigate the electron beam

degradation, (ii) imaging of low temperature transitions with accurate and continuous control of the temperature that allowed single-frame observation of the presence of both the orthorhombic and tetragonal phases in BaTiO<sub>3</sub> system and (iii) magnetic domain wall propagation as a function of temperature, magnetic field and current pulses (100 ns with 100 kHz repetition rate) in the Y<sub>3</sub>Fe<sub>5</sub>O<sub>12</sub> system.

## KEY REFERENCES

- Duchamp, M.; Xu, Q.; Dunin-Borkowski, R.E. Convenient Preparation of High-Quality Specimens for Annealing Experiments in the Transmission Electron Microscope. *Microsc. Microanal.* **2014**, *20*, 1638-1645.<sup>1</sup> *Sample preparation method for MEMS-based operando TEM experiments.*
- Jeangros, Q.; Duchamp, M.; Werner, J.; Kruth, M.; Dunin-Borkowski, R.E.; Niesen, B.; Ballif, C.; Hessler-Wyser, A. In Situ TEM Analysis of Organic–Inorganic Metal-Halide Perovskite Solar Cells under Electrical Bias. *Nano Lett.* **2016**, *16*, 7013-7018.<sup>2</sup> *Degradation mechanism of solar cells is studied in situ by electrical biasing in a TEM.*
- Tyukalova, E.; Duchamp, M. Atomic resolution enabled STEM imaging of nanocrystals at cryogenic temperature. *J. Phys. Mater.* **2020**, *3*, 034006.<sup>3</sup> *Demonstrates implementation of cryogenic STEM to delay degradation caused by radiation damage.*

## Introduction

There are an increasing number of reports on atomic resolution imaging at cryogenic temperatures in transmission electron microscopes (TEMs) to delay the structural changes induced by electron beam irradiation [3-8] or to study low temperature induced reorganization [9-18]. For the former, the main challenge in studying electron beam sensitive emerging materials is to maintain TEM resolution while cooling the specimen to the cryogenic temperature to delay the electron beam induced damage (or radiation damage). For the latter, the imaging of low temperature phases and charge transitions at local scale are related to the ongoing efforts to further understand low temperature phenomena such as quantum materials' phase diagrams [9,11-13,15,17,18] and local pinning of domains walls in ferroelectric [10] and ferromagnetic [14,16] materials. The imaging of temperature-dependent phenomena requires not only accurate continuous and variable temperature control but also application of external stimuli (electric, magnetic, light, etc.) to study devices in *operando* conditions. In section 1.1, we first describe the range of applications of low temperature imaging and spectroscopic capabilities in a TEM with the aim of mitigating electron beam-induced degradation. In section 1.2, we describe the perspective of applications to study low temperature phenomena in a TEM. The following sections, 2.1 and 2.2, describe the state-of-the-art experimental setup and sample preparation techniques for *in situ* and *operando* cryogenic TEM experiments. Section 3 illustrates three examples: low-temperature mitigation of electron beam-induced degradation at atomic resolution (section 3.1), the observation of phase transition in ferroelectric materials (section 3.2), and the pinning of the magnetic domains (section 3.3) over variable temperature range, applied magnetic field, and current pulses.

### 1. Challenges to *in situ* and *operando* TEM experiments at low temperature

#### 1.1 Mitigation of electron beam-induced degradation through cryogenic temperature imaging and spectroscopy

Electron beam-induced degradation mechanisms involve complex physical and chemical processes, namely radiation damage mechanisms: (i) knock-on damage, (ii) thermal damage caused by electron-beam heating, (iii) electrostatic charging, and (iv) radiolysis [19-22]. Knock-on damage for a given material depends on the incident energy of the electron beam and is not affected by specimen temperature. Damage through electrostatic charging, i.e., local depletion of electrons, occurs when the resistivity between ground and the region under observation is high. This mechanism is temperature-dependent in the sense that the specimen conductivity is temperature-dependent. It can be mitigated by using more conductive supports for imaging; for example, a graphene support has been shown to decrease the

electrostatic charging in a liquid cell [23]. The other two degradation mechanisms, thermal damage and radiolysis, have a decreasing cross-section with lower temperature [19]. Thus, imaging at cryogenic temperature has made possible the imaging, at atomic resolution, of Li metal [4] in addition to its spectroscopic characterization using electron energy-loss spectroscopy (EELS) [4, 7]. An alternative approach is to use low dose techniques, at the price of a lower signal-to-noise ratio, which has recently been successfully implemented for imaging organic-inorganic lead halide perovskites [24-26]. For the most challenging specimens, a combination of cryogenic temperature imaging and data post-processing will be needed.

TEM studies using cryogenic temperature to delay the degradation caused by electron beam irradiation have regained interest in recent years due to the development of (i) imaging [27] and spectroscopy [28] at atomic resolution that has resulted in an increase of the electron dose compared to conventional imaging techniques; (ii) new materials that are very sensitive to electron beam irradiation, such as Li-based compounds used for battery applications [3-6, 8], metal-organic frameworks [25], organic-inorganic lead halide perovskites [24-26], and materials for electrocatalytic reactions [3]; and (iii) new TEM holders and numerical analysis techniques that allow imaging beam sensitive materials at cryogenic temperature which could not otherwise be imaged [28-30, 42].

### **1.2 *In situ* and *operando* TEM experiments in a continuous and variable temperature range**

To study low temperature transition phenomena at local scale in a TEM, an accurate and tunable control of the temperature is needed – typically to follow *in situ* a TEM the microstructural reorganization happening across phase transitions [9-17]. In addition, thermally activated processes and their interactions with devices' performance need to be studied *operando*, i.e., with application of external stimuli. Moreover, the *in situ* and *operando* TEM experiments require the observation of devices in their native state and under operating conditions. For biological experiments, this has been achieved by moving from cryo-TEM [31] to *in situ* experiments in a liquid environment inside the TEM [33]. For material science, the observation of devices and materials at various temperatures, under external stimulus (electrical, magnetic, light, etc.), or ideally with a combination of both is still challenging [2, 34-41].

## **2. MEMS-based TEM holder to reach atomic resolution and perform *operando* studies at low temperature**

### **2.1 Low temperature TEM holder experimental setup**

Most of the low temperature *in situ* TEM measurements reported to date have been realized using a cryogenic TEM holder holding 3 mm grids. Unfortunately, the drift of such a holder has made it difficult to record high resolution images, which have been achieved through complex data post-processing to enhance the signal-to-noise ratio and to correct for specimen drift [42, 43]. Other drawbacks are the limited available time to perform the experiments due to the small volume of the liquid nitrogen dewar, the formation of ice during experiments which limits the spatial and spectroscopic resolution, and the difficulty in precisely controlling the temperature in a continuous way. Despite the limitations of this technology, the imaging of Li metal [5] and phase transition [13] at cryogenic temperature was achieved. To overcome these drawbacks, a MEMS-based TEM holder was developed by HennyZ (Fig. 1a) [29]. In brief, this holder is cooled down by immersing a copper braid in a 4.5-liter liquid nitrogen dewar fixed to the TEM column that prevents vibration which would limit the ultimate resolution. Through a thermally conductive rod, the tip of the holder is cooled down to the lowest achievable temperature. The specimen drift is tackled by using active temperature regulation near the tip of the holder, allowing thermal isolation between the cold tip where the specimen sits and the holder rod which is in contact with the TEM column. An image of the tip of the holder is shown in the inset of Fig. 1a, where the location of the MEMS chip (1), the six needles contacting the MEMS chip (2), and the active temperature regulator (3) are indicated. After the tip (along with the specimen) has reached its lowest temperature, corresponding to a thermal equilibrium between the cold transferred from the copper braid through the holder and the radiation inside the TEM that tends to increase the tip's temperature, the sample drift is

decreased to below 1 nm/min. Such stability allows sub-Angstrom resolution imaging in a single frame without further averaging or other post-processing treatment (Fig. 1b). The temperature at the specimen location is controlled by a heating element directly patterned onto the MEMS-chip, similar to what is done for elevated temperature MEMS-based TEM holders [43, 44]. The temperature at the specimen location is varied by passing a current through a Pt track on the MEMS chip, with the temperature obtained by measuring the resistance across the Pt heating element. A great advantage of the accurate and fast temperature control allowed by the MEMS chip is the possibility of increasing the specimen temperature to sublimate any ice that may have deposited onto the samples, a problem which had also been limiting the overall experimental time with a conventional 3 mm grid cryogenic holder. Two other advantages of the six-contact double tilt holder available in our laboratory are the possibilities of specimen alignment along a zone axis and electrically contacting the devices deposited on the MEMS chips by following the specimen preparation procedure detailed elsewhere [1, 46]

## 2.2 Sample preparation

*In situ* and *operando* TEM experiments require the preparation of electron transparent specimens and their transfer on support enabling the low temperature characterization. Most of the studies reported so far are based on the observation of nanoparticles or 2D materials which can be directly deposited on conventional substrates without further processing [3]. When bulk samples or devices are of interest, an electron transparent TEM lamella should be extracted, possibly at the location of interest. Lamellae, these days, are extracted using focused ion beam (FIB) milling combined with *in situ* lift-off in a SEM-FIB workstation and transferred, either to a dedicated copper grids [46, 47] or directly onto MEMS-based chips [1]. Using such an approach, we have transferred electron transparent TEM lamellae from bulk  $\text{BaTiO}_3$  and  $\text{Y}_3\text{Fe}_5\text{O}_{12}$  crystals to MEMS chips. A typical image of an electron transparent lamella electrically contacted on a MEMS chip is shown Fig. 1c, with the red arrow indicating the location of the lamella.

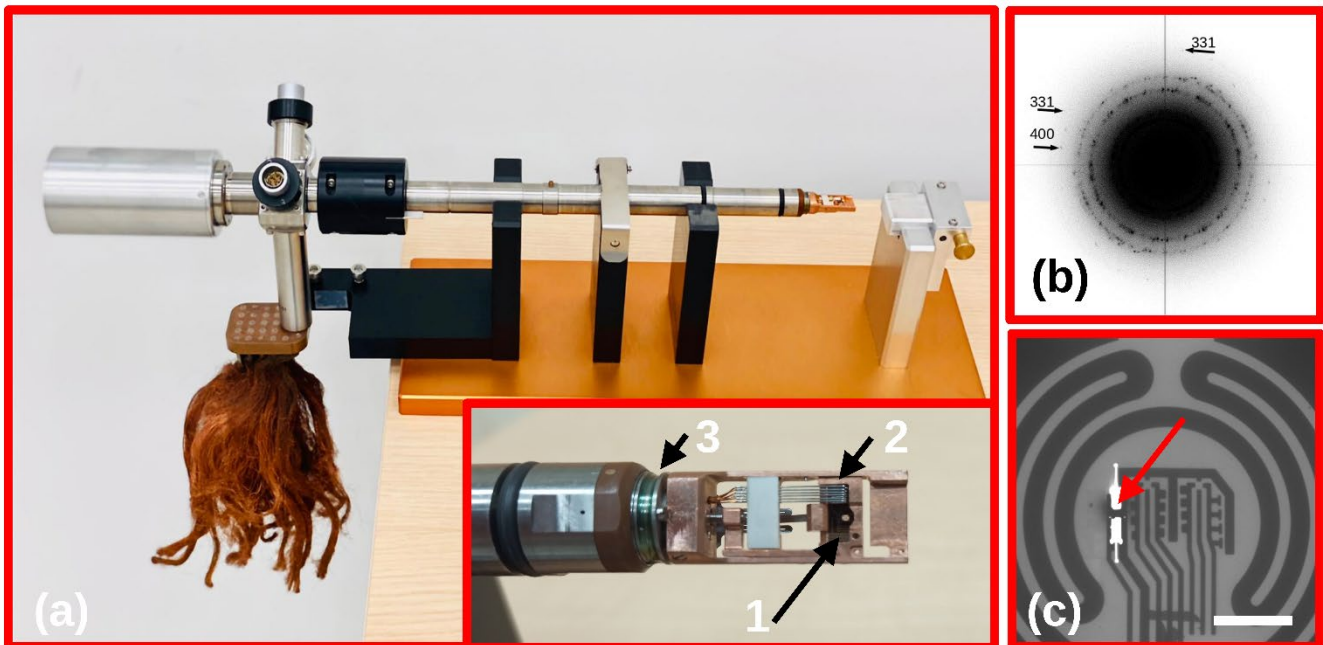


Figure 1. (a) Photograph of the HennyZ liquid-nitrogen double-tilt specimen holder used for low temperature investigations. A high magnification image of the holder tip is shown as an inset, the numbers 1, 2 and 3 indicate the location of the MEMS chip, the six needles for electrical biasing and the active temperature regulator, respectively. (b) Fast Fourier Transform of a single frame high resolution TEM image where the 400 and 331 Au reflections are indicated by the respective arrows. (c) Low magnification STEM micrograph of the  $\text{Y}_3\text{Fe}_5\text{O}_{12}$  lamella deposited onto a MEMS chip and observed at low temperature (see section 3.3). The scale bar is 50  $\mu\text{m}$ .

### 3. Applications

#### 3.1 Atomic resolution imaging of electron beam sensitive materials at cryogenic temperature to mitigate radiation damage

A strong focus in current energy research is towards the development of sustainable, inexpensive, and high energy density storage systems. Li-ion batteries are efficient devices for electrical energy storage, having high energy and power density compared with other type of batteries. A promising alternative to the conventional cathode material is  $\text{LiNi}_{0.5}\text{Mn}_{1.5}\text{O}_4$  (LNMO) due to its possible use for new generation high-voltage Li-ion batteries. However, various factors including the oxidation states of ions, atomic coordination of the Mn and Ni cations, and the morphology of the particles influence the performance of LNMO as a cathode material [49, 50], preventing the widespread commercialization of LNMO cathode in Li ion-based batteries.

Previous results obtained using the high-angle annular-dark field scanning-TEM (HAADF-STEM) imaging technique have shown the presence of different crystallographic phases at different states of charge of LNMO-based batteries, which may be the origin of the capacity fading upon cycling. During the discharge, apart from pristine spinel and  $\text{Mn}_3\text{O}_4$ -phases, the rocksalt-like phase has been observed on the subsurface. However, rocksalt and intermediate ( $\text{Mn}_3\text{O}_4$ -like) phases were not observed by XRD and no correlation between those phases and cell performance were found [51]. On the contrary, the phase transformation from spinel to rocksalt phase was observed due to electron beam irradiation in  $\text{LiMn}_2\text{O}_4$ , which has the same spinel structure as LNMO [52]. It has been shown that upon continuous electron-beam irradiation during HAADF-STEM imaging, Mn/Ni atoms move first into tetrahedral sites, and afterwards into empty octahedral sites forming the rocksalt phase (Fig. 2g). Thus, more research is needed in order to investigate the stability of the LNMO cathode material under the electron beam irradiation, and to find a correlation between evolution of the LNMO microstructure and its charging/discharging behavior during battery operation.

Figures 2(a and b) present the evolution of the atomic structure of a discharged LNMO particle under HAADF-STEM imaging at room temperature. The estimated total dose for the first image of the series (Fig. 2a) is  $1.1 \times 10^6 \text{ e}^- \cdot \text{\AA}^{-2}$ , that is defined as the electron dose used to align the particle into the zone axis and to record the image. The nanoparticle comprises the spinel structure over the whole area being imaged. A consecutively acquired image, with a total dose of  $2.3 \times 10^6 \text{ e}^- \cdot \text{\AA}^{-2}$  (Fig. 2b) shows the presence of an additional contrast in the octahedral site. This new structure corresponds to the rocksalt phase, induced by electron beam irradiation.

Similarly, two consecutive images of LNMO nanoparticles were recorded at cryogenic temperature (Figs. 2d,e) by following the same protocol as for images acquired at room temperature (Figs. 2a,b). Under cryogenic imaging conditions, there is no extra contrast visible at the octahedral sites, indicating that the spinel phase is preserved.

Series of electron energy-loss spectra (EELS) recorded at room temperature (Fig. 2c) and at cryogenic temperature (Fig. 2f) at the O K-edge shows the evolution of the fine structure versus total electron dose. For the series recorded at room temperature, the intensity of the pre-peak below 530 eV decreases and the main peak at  $\sim 540$  eV shifts toward higher energies with increasing total electron dose. For a total electron dose of  $1.1 \times 10^6 \text{ e}^- \cdot \text{\AA}^{-2}$  (used to record Fig. 2a) the electronic structure of the O K-edge is strongly modified as compared to the pristine spectra recorded at  $2 \times 10^5 \text{ e}^- \cdot \text{\AA}^{-2}$ . Despite the observation of the spinel structure at a total dose of  $1.1 \times 10^6 \text{ e}^- \cdot \text{\AA}^{-2}$ , the atomic environment has already been modified by the electron irradiation at room temperature. Conversely, the EELS series recorded at cryogenic temperature shows the O K-edge is still in its pristine state for  $1.1 \times 10^6 \text{ e}^- \cdot \text{\AA}^{-2}$  and lightly affected for doses up to  $5 \times 10^7 \text{ e}^- \cdot \text{\AA}^{-2}$ , which is more than one order of magnitude larger than the dose used to record the second HAADF-STEM image at cryogenic temperature.

This delay in electron beam-induced degradation at cryogenic temperature offers the possibilities of studying the pristine structure of Li-based materials and correlating the local atomic arrangement with electrochemical performance and capacity fade.

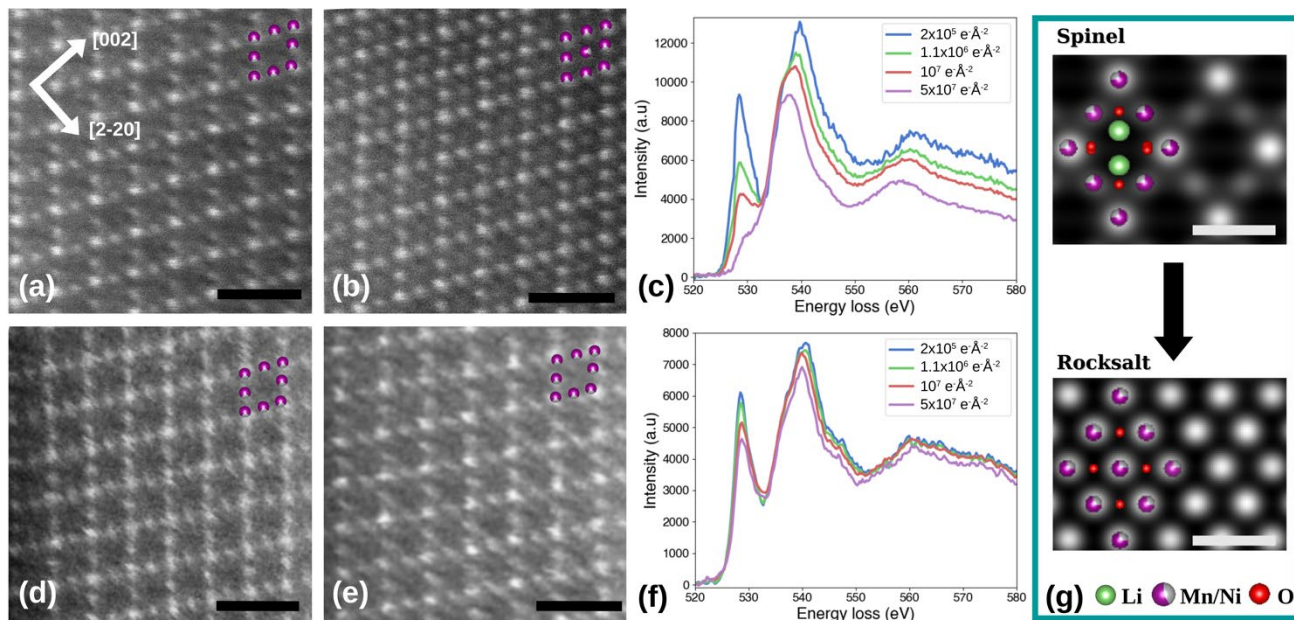


Figure 2. (a, b, d, e) HAADF-STEM images of discharged  $\text{LiNi}_{0.5}\text{Mn}_{1.5}\text{O}_4$  nanoparticle imaged along the  $[110]$  orientation recorded with an electron-beam energy of 200 keV using a dwell time of 16  $\mu\text{s}$ , a pixel size of 21 pm and inner and outer collection angles of 68 and 280 mrad, respectively. (a-b) Images recorded at room temperature (a) with a total electron dose of  $1.1 \times 10^6 \text{ e}^- \cdot \text{\AA}^{-2}$  and (b) consecutively to a with a total dose of  $2.3 \times 10^6 \text{ e}^- \cdot \text{\AA}^{-2}$ . (d-e) Images recorded at cryogenic temperature (d) with a total electron dose of  $1.1 \times 10^6 \text{ e}^- \cdot \text{\AA}^{-2}$  and (e) consecutively to image d with a total dose of  $2.3 \times 10^6 \text{ e}^- \cdot \text{\AA}^{-2}$ . (c, f) Series of EELS spectra recorded at the O K-edge at (c) room temperature and at (f) cryogenic temperature. The total electron dose ranging from  $2 \times 10^5 \text{ e}^- \cdot \text{\AA}^{-2}$  to  $5 \times 10^7 \text{ e}^- \cdot \text{\AA}^{-2}$ . (g) HAADF-STEM image simulations done with Dr. Probe [53] and the overlay of the atomic structures of the proposed structural transformation under electron beam irradiation from the spinel to the rocksalt structure. The scale bars are (a, b, d, e) 10  $\text{\AA}$  and (g) 5  $\text{\AA}$ .

### 3.2 Mapping of the ferroelectric phase diagram of $\text{BaTiO}_3$ across continuously variable temperatures

$\text{BaTiO}_3$  is a prototypical ferroelectric system that exhibits several phase transitions. Above the Curie temperature ( $T_c \sim 393 \text{ K}$ ), it is centrosymmetric ( $\text{Pm-3m}$ ) and it becomes tetragonal ( $\text{P4mm}$ ) upon cooling to room temperature. Further cooling to  $\sim 278 \text{ K}$  induces a transition to the orthorhombic phase ( $\text{Amm2}$ ) whereas at  $\sim 183 \text{ K}$  the final transition to the rhombohedral phase ( $\text{R3m}$ ) is induced. All three ferroelectric phases exhibit spontaneous polarization in different crystallographic directions and thus the domain structure depends highly on the temperature. In the tetragonal, room temperature phase, the spontaneous polarization is directed parallel to the facet of the pseudocubic (PC) unit cell of the perovskite structure (along  $[001]_{\text{PC}}$ ), and reorganizes along a face diagonal in the orthorhombic phase (in the  $[011]_{\text{PC}}$  direction) and the body diagonal ( $[111]_{\text{PC}}$  direction) in the rhombohedral phase. Additionally, due to the piezoelectric properties of  $\text{BaTiO}_3$ , the domain structure at different temperatures is highly sensitive to the sample geometry, the mechanical stress, and possible external electric fields [543]. This redistribution of the ferroelectric domains across the different phases and their interplay with local interfaces, local defects, and geometrical constraints is of particular importance for device engineering. However, progress on understanding such complex dynamic phenomena in ferroelectrics has been limited by available techniques.

Here, we are concerned with the phase diagram of single crystalline BaTiO<sub>3</sub> as a function of temperature, with particular focus on the relative stability of the low-temperature phases. We take advantage of the versatility of the continuously variable low temperature MEMS-based holder to follow the formation of the ferroelectric domains in real space. Temperature cycles from the high temperature phase down to ~200 K are performed inside the TEM while imaging the redistribution of the ferroelectric domains. The montage of the bright-field (BF-)TEM micrographs corresponding to this temperature cycle is shown in Fig. 3 and the associated video is provided in the supporting information. The dark lines in most images are so-called bending contours due to the slightly varying diffraction conditions across the sample and are the only visible contrast in the cubic paraelectric state observed above T<sub>c</sub> (400 K in Fig. 3). For the images below T<sub>c</sub>, the characteristic diffraction contrast from the domain walls can easily be separated from the background bending contours.

Upon cooling, the structure becomes tetragonal with the polarization being along the [100]<sub>PC</sub> direction with 90° domain walls becoming visible (392 K in Fig. 3). At 324 K, both 90° and 180° domain walls are visible in the same TEM micrograph. Further cooling in the tetragonal phase induces the reorganization of the domain structure to fully contain 180° domain walls. This appearance of tetragonal phase 180° domain walls close to room temperature is associated with the constrained geometry of the system since the specimen is attached on the MEMS chip on the two sides along the [100]<sub>PC</sub> crystallographic direction [40]. At around 249 K, a subtle transition to the orthorhombic phase is induced and it is followed by similar domain structure although this time the polarization direction is along the [110]<sub>PC</sub>. Even though a similar domain wall shape is retained after the transition, the rotation of the polarization indicates that the domain walls in the orthorhombic phase, if considered neutral, are 90°. At the lowest temperature accessed in this experiment, 200 K, the orthorhombic domain walls become less well-defined, suggesting that the final phase transition to the rhombohedral phase is imminent.

Upon heating, the orthorhombic to tetragonal phase transition occurs at ~260 K which is ~10 K higher as compared to the temperature upon cooling. Close to room temperature, the 180° domain walls in the tetragonal phase obtained upon heating have a larger periodicity as compared to the domain walls obtained upon cooling. Their periodicity is linked to the rearrangement of local stresses. Additionally, the micrographs show that upon heating the 180° domain walls of the tetragonal phase are pinned at the same sites as their low temperature orthorhombic counterpart. It is interesting as this effect was not observed upon cooling, i.e., the domains of the tetragonal phase have merged upon cooling but do not split upon annealing across the phase transition to the orthorhombic structure. The increase of the 180° domain wall density happens at temperatures above ~325 K. This behavior shows the importance of studying the displacements of the domain walls across temperature phase transitions at nanometer scales *in situ* in a TEM. Similarly, the change of the tetragonal phase from 180° to 90° domain walls is observed at ~10 K higher temperature upon heating as compared with its redistribution upon cooling. A similar hysteresis is observed from the tetragonal to the cubic phase.

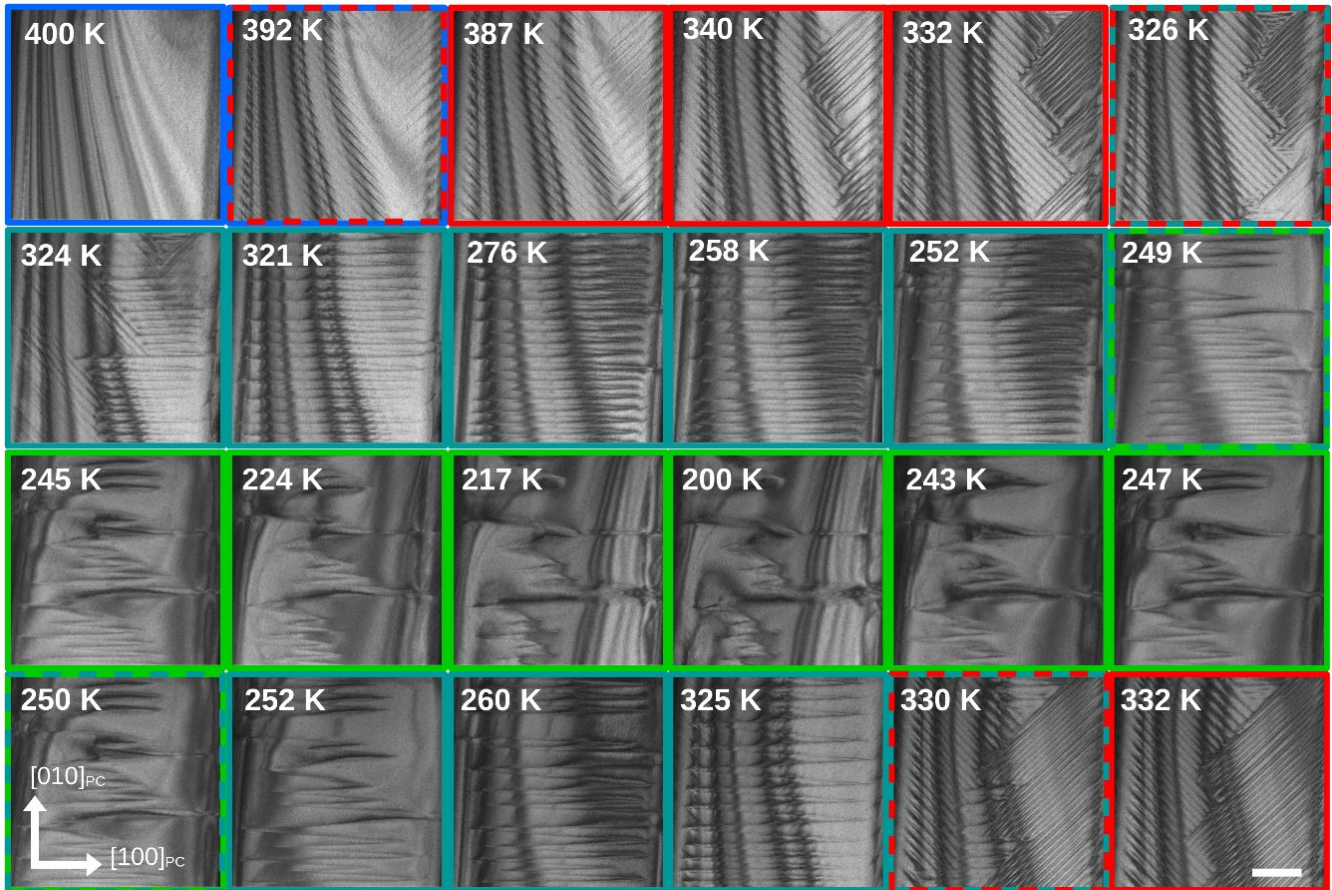


Figure 3. BF-TEM micrographs of a temperature cycle of BaTiO<sub>3</sub> (heating from high temperature, cooling to the lowest point (200 K) and heating back to high temperature sequentially). The scale bar is 400 nm.

### 3.3 Cryogenic TEM imaging of magnetic domain dynamics *in situ* in a variable temperature range and *operando*

*In situ* low temperature magnetic domain studies at nanoscale play a major role to unlock the fundamental physics of magnetism and its associated effects. The domain structure of magnetic thin films is generally analyzed using magnetic force microscopy (MFM), which is sensitive only to stray fields near the surface [57], and magneto optic Kerr effect (MOKE) microscopy [58], which has a limited spatial resolution. Lorentz microscopy is an alternative technique which can provide qualitative information about the magnetization within the material and can be used to study the domain wall propagation [9,60]. Here, we perform Lorentz TEM imaging at cryogenic temperature to investigate the magnetic domains in the ferrimagnetic insulator Y<sub>3</sub>Fe<sub>5</sub>O<sub>12</sub> [61].

The monocrystalline epitaxial 10 μm-thick Y<sub>3</sub>Fe<sub>5</sub>O<sub>12</sub> films were grown on Gallium Gadolinium Garnet (GGG) substrates using liquid phase epitaxy (LPE) technique [62, 63] and covered by a 5.5 nm-thick Pt layer and a 200 nm-thick Al<sub>2</sub>O<sub>3</sub> dielectric layer (Fig. 4a). The TEM was operated in a magnetic field free condition where the objective lens was switched off (Lorentz mode) [9,56,57,59,60]. Figure 4b shows the in-focus image of the Y<sub>3</sub>Fe<sub>5</sub>O<sub>12</sub> lamella, while Fig. 4c and Fig. 4d show underfocused and overfocused Lorentz images, respectively. Figure 4c has a line with a bright contrast in the middle of the lamella and a dark contrast line at the bottom of the lamella. An opposite contrast to Fig. 4c is seen in Fig. 4d indicating that the lines correspond to magnetic domain walls [64].

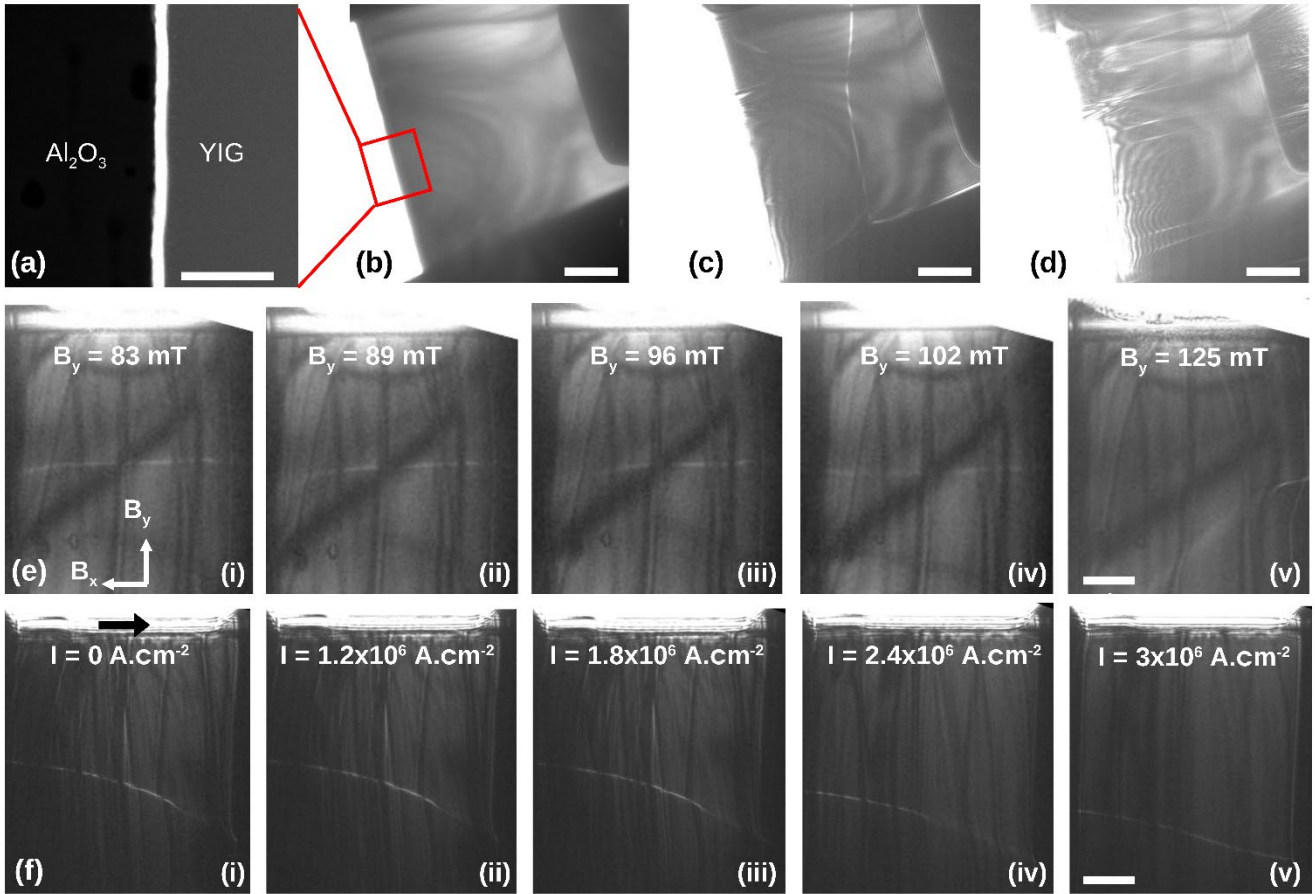


Figure 4. (a) STEM image of the top  $\text{Al}_2\text{O}_3/\text{Pt}/\text{Y}_3\text{Fe}_5\text{O}_{12}$  interface, (b) in-focus, (c) under-focus and (d) over-focused Lorentz TEM images showing magnetic domain walls in  $\text{Y}_3\text{Fe}_5\text{O}_{12}$  (e, i-v) Micrograph series recorded with increasing magnetic field. (f, i-v) Micrograph series recorded while applying current pulses for increasing current densities. The associated video is provided in the supporting information. The scale bars are (a) 50 nm and (b – f) 1  $\mu\text{m}$ .

The *operando* studies were conducted on  $\text{Y}_3\text{Fe}_5\text{O}_{12}$  lamella (1) by applying the magnetic field near the sample which was generated by passing the current through the objective lens, (2) by applying a pulsed current through the Pt layer, and (3) by changing the temperature of the sample. The coercive field for the  $\text{Y}_3\text{Fe}_5\text{O}_{12}$  thin films is very small, thus the domain walls are expected to move easily (in-plane saturation field  $H_s=30$  Oe [59]). Figures 4e(i-v) show the switching between two pinning sites by varying the applied magnetic field. Even though the magnetic field of the objective lens is orthogonal to the MEMS chip, the  $\text{Y}_3\text{Fe}_5\text{O}_{12}$  lamella experiences a small in-plane magnetic field due to the 13-degree tilt of the lamella with respect to the MEMS chip. In the absence of any external magnetic field, a pinned domain wall (with a bright contrast) was found  $\sim 2$   $\mu\text{m}$  below the top interface. By increasing the magnetic field, the domain wall was found to move from one pinned location to a second one as made visible in Figs. 4e (i, v). This change was reversible over 10 cycles of external magnetic field (from positive to negative tilts or vice versa).

Figure 4f show the motion of magnetic domain walls versus pulsed current density (100 ns pulses with 100 kHz repetition rate). The current pulse is applied through the Pt layer sandwiched in between the  $\text{Y}_3\text{Fe}_5\text{O}_{12}$  and  $\text{Al}_2\text{O}_3$  layers. The applied charge current in the Pt layer will generate the spin current due to the spin Hall effect [60, 61]. The generated spin current will exert the torque on the magnetization direction of  $\text{Y}_3\text{Fe}_5\text{O}_{12}$  thin film which allows control of the domain wall motion *operando* inside the TEM. We observe the domain wall motion is well visible above a current density of  $2.4 \times 10^6$   $\text{A.cm}^{-2}$ ,

compared with a  $5 \times 10^6$  A.cm<sup>-2</sup> current density reported in *ex situ* experiments [62]. This will allow control of the position of a magnetic domain wall with an electric current more suitable for new types of non-volatile memory and logic devices [63, 64]. Moreover, our measurement will also be useful to understand the intrinsic pinning sites available in the magnetic materials due to the magnetic anisotropy, which affects the magnetic domain propagation [65].

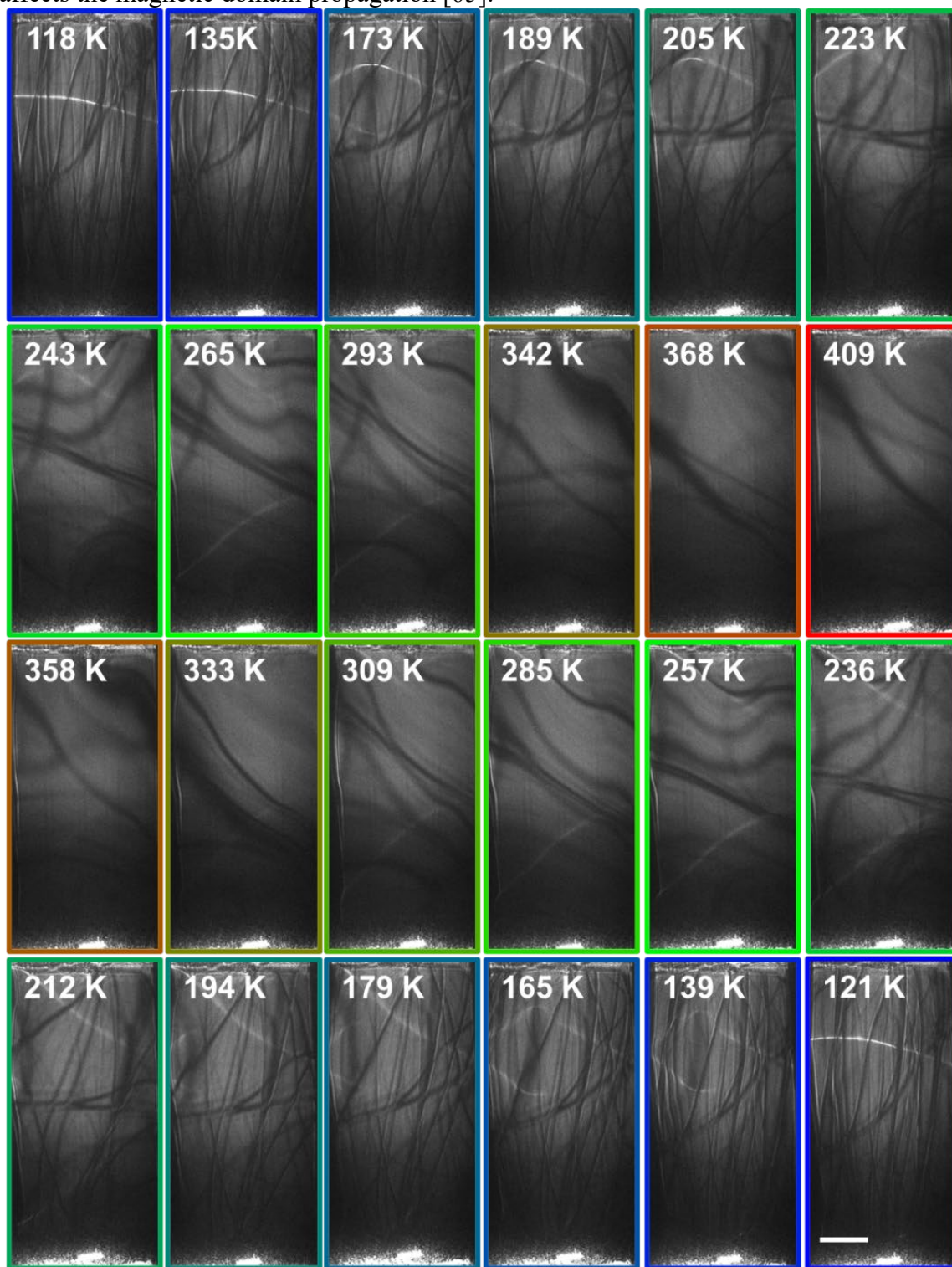


Figure 5. A montage of TEM images in Lorentz mode showing the motion of domain walls in  $Y_3Fe_5O_{12}$  with temperature. The associated video is provided in the supporting information. The scale bar is 1  $\mu$ m.

Finally, we have also studied the motion of the domain walls with the temperature. The temperature was varied from 118 K to 409 K and then back to 121 K (Figs. 5). The phase transition of  $\text{Y}_3\text{Fe}_5\text{O}_{12}$  from ferromagnetic to paramagnetic state was studied by increasing the temperature of the sample while observing its magnetic structure. Different magnetic states are found with temperature, namely a low temperature configuration is found below 130 K-140 K, with a strong contrast of the domain wall. A second, higher temperature state, is found in the 140 K to 300 K range with a weaker contrast than in the low temperature state. At temperatures near  $T_c$ , the signal from the magnetic domains weakens and disappears toward the bottom of the lamella. The transition between the two low temperature states is shifted more than 20 K when comparing the cooling and the heating series. Moreover, the domain seems to be pinned at this location, reappearing at the same location while cooling back to 300 K and being pinned till about 236 K.

#### 4. Conclusion and Perspectives

As this Account has demonstrated, the atomic resolution STEM imaging in single frame at cryogenic temperature is possible for randomly dispersed nanoparticles, thanks to the double-tilt MEMS-based cryogenic holder recently made available. Further, cryogenic temperature imaging allows delaying the electron beam induced degradation of LMNO, revealing its true micro-structure. More subtle changes in the local atomic environment of the oxygen atoms versus electron dose were probed by EELS, showing that even if the micro-structure seems to be in its pristine state when imaged at room temperature, the O K fine structure is altered for doses as low as  $10^6 \text{ e}^- \cdot \text{\AA}^{-2}$ , typical for high-resolution HAADF-STEM imaging.

The second aspect demonstrated in this Account is the possibility to image ferroelectric domain transformation and magnetic domain wall propagation versus temperature varied in continuous manner. Moreover, the temperature modulation can be combined with other stimuli applied to the specimen under observation. As an example, we have imaged the displacement of magnetic domain walls by applying magnetic field and pulsed current stimuli. The demonstration of these initial capabilities is a promising step toward the study of *operando* AC phenomena in a continuous cryogenic temperature range. Based on these results, the challenges of combining temperature, magnetic, and electrical stimuli are expected to soon be possible *in situ* and *operando* in a TEM.

#### Notes

The authors declare no competing financial interest.

#### Biographies

**Elizaveta Tyukalova** received a Master's degree in 2016 from the Moscow Institute of Physics and Technology, Moscow, Russia, currently Ph.D. candidate at NTU. Her research focuses on applications of *in situ* and *operando* TEM techniques to materials and devices for energy applications.

**Joseph Vimal Vas** received a Ph.D degree in 2018 from the Indian Institute of Science, Bangalore. , currently research fellow at the NTU working in field of spintronics, domain wall propagation and advanced TEM techniques for *in situ* and *operando* studies.

**Reinis Ignatans** received a Master's degree from the University of Latvia (2015), currently he is aPh. D candidate at EPFL focusing on the study of the dynamic behavior of ferroelectric phases using heating and biasing stimuli in a TEM.

**Aaron David Mueller** received a Ph.D degree in 2019 from NTU. He is currently research fellow at NTU, working on the fabrication of MEMS, 2D material devices, and electrostatic electron beam shaping in the TEM.

**Rohit Medwal** received a Ph.D. degree in 2014 from university of Delhi, India. Thereafter, he pursued a research fellow position at Kyushu institute of technology, Japan working on the spin-transport

phenomena. He is currently research fellow at NTU working on spin-Hall effect and spin pumping for spin orbit torques switching and *in situ* and *operando* TEM studies.

**Masaaki Imamura** received his Dr. Eng. Degree in 1979, emeritus professor since 2016 from Kyushu University, Fukuoka, Japan. He is studying the thermoelectric voltage in spin thermoelectric generator fabricated from liquid phase epitaxial iron garnet films. His interests include the magneto-optics for II-VI diluted magnetic semiconductors.

**Hironori Asada** received a Dr. Eng. degree in 1991 from Kyushu University, Japan. Currently, he is Professor of Graduate school of Sciences and Technology for Innovation, Yamaguchi University, Ube, Japan. His research interests include magnetic materials for spintronics and magnetic device fabrications.

**Yasuhiro Fukuma** received a PhD in 2002 from Yamaguchi University, Japan on the growth of IV-VI ferromagnetic semiconductors and the characterization of their magnetic properties. After postdoctoral research at Yamaguchi Prefectural Industrial Technology Institute and at University of Alabama, he became deputy team leader at RIKEN in 2010. He joined Kyushu Institute of Technology in 2012 and is currently Professor in department of Physics and Information Technology. He is working on material sciences and nanodevices for spintronic applications.

**Rajdeep Singh Rawat** received a Ph.D in 1994 from University of Delhi, India and is currently Professor in Physics in NTU. He works in multi-disciplinary field of experimental plasma physics and material science, spintronics with particular interest on high charge to spin conversion and vice versa in Rashba interfaces, high-Z materials and alloys.

**Vasiliki Tileli** received a Ph.D in 2009 from the State University of New York. She then completed her Marie Curie individual Fellowship at Imperial College London. She is currently assistant Professor at EPFL where, with her group, she studies on a fundamental level the nanoscale properties of functional materials using *in situ* TEM techniques.

**Martial Duchamp** received a Ph. D in 2011 from EPFL. During in two consecutive research fellow positions at the Technical University of Denmark and Forschungszentrum Juelich, Germany is specialized in high-resolution electron microscopy imaging, spectroscopy and in the development of *in situ* techniques. He is currently assistant Professor at NTU, working on the development of *in situ* and *operando* TEM methods to investigate new generation of materials and devices.

## ACKNOWLEDGMENTS

E. T., A. D. M. and M. D. acknowledge the ministry of Education (MOE) Singapore for the support through MOE Tier 1 RG87/19 (S) and Nanyang Technological University for the support through the MSE starting grant. R. S. Rawat acknowledges MOE, Singapore for the support through MOE Tier 2 Grant, ARC-1/17 RSR (MOE2017-T2-2-129) and NRF, Singapore for the support through CRP Grant, CRP21-2018-0093. R. I. and V. T. acknowledge support by the Swiss National Science Foundation (SNSF) under award no. 200021\_175711. Transmission electron microscopy imaging was performed at the Facility for Analysis, Characterization, Testing and Simulation (FACTS) in Nanyang Technological University, Singapore.

## SUPPORTING INFORMATION

Video 1: Video associated to montage of the bright-field BF-TEM micrographs shown in Figs. 3.

Video 2: Video associated to the micrograph series recorded while applying current pulses for increasing current densities shown in Figs. 4 (f).

Video 3: Video associated to the montage of TEM images in Lorentz mode showing the motion of domain walls in  $Y_3Fe_5O_{12}$  with temperature shown in Figs. 5.

## REFERENCES

- (1) Duchamp, M.; Xu, Q.; Dunin-Borkowski, R. E. Convenient Preparation of High-Quality Specimens for Annealing Experiments in the Transmission Electron Microscope. *Microscopy and Microanalysis*. **2014**, 20, 1638–1645.
- (2) Jeangros, Q.; Duchamp, M.; Werner, J.; Kruth, M.; Dunin-Borkowski, R. E.; Niesen, B.; Ballif, C.; Hessler-Wyser, A. In Situ TEM Analysis of Organic–Inorganic Metal-Halide Perovskite Solar Cells under Electrical Bias. *Nano Letters*. **2016**, 16, 7013–7018.
- (3) Tyukalova, E.; Duchamp, M. Atomic Resolution Enabled STEM Imaging of Nanocrystals at Cryogenic Temperature. *J. Phys. Mater.* **2020**, 3, 034006.
- (4) Otsuka, Y.; Shimizu, Y.; Tanaka, I. Beam Damage Suppression of Low- Porous Si-O-C Films by Cryo-Electron-Energy Loss Spectroscopy (EELS). *Journal of Electron Microscopy*. **2009**, 58, 29–34.
- (5) Li, Y.; Li, Y.; Pei, A.; Yan, K.; Sun, Y.; Wu, C.-L.; Joubert, L.-M.; Chin, R.; Koh, A. L.; Yu, Y.; Perrino, J.; Butz, B.; Chu, S.; Cui, Y. Atomic Structure of Sensitive Battery Materials and Interfaces Revealed by Cryo–Electron Microscopy. *Science*. **2017**, 358, 506–510.
- (6) Zachman, M. J.; Tu, Z.; Choudhury, S.; Archer, L. A.; Kourkoutis, L. F. Cryo-STEM Mapping of Solid–Liquid Interfaces and Dendrites in Lithium-Metal Batteries. *Nature*. **2018**, 560, 345–349.
- (7) Ayoola, H. O.; Li, C.-H.; House, S. D.; Bonifacio, C. S.; Kisslinger, K.; Jinschek, J.; Saidi, W. A.; Yang, J. C. Origin and Suppression of Beam Damage-Induced Oxygen-K Edge Artifact from  $\gamma$ -Al<sub>2</sub>O<sub>3</sub> Using Cryo-EELS. *Ultramicroscopy*. **2020**, 219, 113127.
- (8) Zhang, Z.; Yang, J.; Huang, W.; Wang, H.; Zhou, W.; Li, Y.; Li, Y.; Xu, J.; Huang, W.; Chiu, W.; Cui, Y. Cathode-Electrolyte Interphase in Lithium Batteries Revealed by Cryogenic Electron Microscopy. *Matter*. **2021**, 4, 302–312.
- (9) Chen, C. H.; Gibson, J. M.; Fleming R. M. Direct Observation of Charge-Density-Wave Discommensurations and Dislocations in 2H-TaSe<sub>2</sub> Physical Review Letters **1981**, 47, 723.
- (10) Lemmens, H.; Richard, O.; Van Tendeloo, G.; Bismayer U. Microstructure and phase transitions in Pb(Sc<sub>0.5</sub>Ta<sub>0.5</sub>)O<sub>3</sub> Journal of Electron Microscopy **1999**, 48, 843–847.
- (11) McQueen, T. M.; Williams, A. J.; Stephens, P. W.; Tao, J.; Zhu, Y.; Ksenofontov, V.; Casper, F.; Felser, C.; Cava R. J. Tetragonal-to-Orthorhombic Structural Phase Transition at 90 K in the Superconductor Fe<sub>1.01</sub>Se Physical Review Letters **2009**, 103, 057002.
- (12) Phatak, C.; Petford-Long, A. K.; Zheng, H.; Mitchell, J. F.; Rosenkranz, S.; Norman, M. R. Ferromagnetic Domain Behavior and Phase Transition in Bilayer Manganites Investigated at the Nanoscale. *Phys. Rev. B*. **2015**, 92, 224418.
- (13) Hovden, R.; Tsen, A. W.; Liu, P.; Savitzky, B. H.; El Baggari, I.; Liu, Y.; Lu, W.; Sun, Y.; Kim, P.; Pasupathy, A. N.; Kourkoutis, L. F. Atomic Lattice Disorder in Charge-Density-Wave Phases of Exfoliated Dichalcogenides (1T-TaS<sub>2</sub>). *Proc Natl Acad Sci USA*. **2016**, 113, 11420–11424.

- (14) Yu, X.; Morikawa, D.; Tokunaga, Y.; Kubota, M.; Kurumaji, T.; Oike, H.; Nakamura, M.; Kagawa, F.; Taguchi, Y.; Arima, T. h.; Kawasaki, M.; Tokura Y. Current-Induced Nucleation and Annihilation of Magnetic Skyrmions at Room Temperature in a Chiral Magnet *Adv. Mater.* **2017**, 29, 1606178.
- (15) Zhao, W.; Li, M.; Chang, C. Z.; Jiang, J.; Wu, L.; Liu, C.; Moodera, J. S.; Zhu, Y.; Chan, M .H. W. Direct imaging of electron transfer and its influence on superconducting pairing at FeSe/SrTiO<sub>3</sub> interface *Science advances* **2018**, 4, eaao2682.
- (16) Shibata, K.; Tanigaki, T.; Akashi, T; Shinada, H., Harada, K.; Niitsu, K.; Shindo, D.; Kanazawa, N.; Tokura, Y.; Arima T-h Current-Driven Motion of Domain Boundaries between Skyrmion Lattice and Helical Magnetic Structure. *Nano letters.* **2018**, 18, 929-933.
- (17) El Baggari, I.; Savitzky, B. H.; Admasu, A. S.; Kim, J.; Cheong, S.-W.; Hovden, R.; Kourkoutis, L. F. Nature and Evolution of Incommensurate Charge Order in Manganites Visualized with Cryogenic Scanning Transmission Electron Microscopy. *Proc Natl Acad Sci USA.* **2018**, 115, 1445–1450.
- (18) El Baggari, I.; Sivadas, N.; Stiehl, G. M.; Waelder, J.; Ralph, D. C.; Fennie, C. J.; Kourkoutis, L. F. Direct Visualization of Trimerized States in 1T'-TaTe<sub>2</sub> Physical Review Letters **2020**, 125, 165302.
- (19) Egerton, R. F.; Li, P.; Malac, M. Radiation Damage in the TEM and SEM. *Micron.* **2004**, 35, 399–409.
- (20) Egerton, R. F. Radiation Damage to Organic and Inorganic Specimens in the TEM. *Micron.* **2019**, 119, 72–87.
- (21) Meyer, J. C.; Eder, F.; Kurasch, S.; Skakalova, V.; Kotakoski, J.; Park, H. J.; Roth, S.; Chuvilin, A.; Eychsen, S.; Benner, G.; Krashennnikov, A. V.; Kaiser, U. Accurate Measurement of Electron Beam Induced Displacement Cross Sections for Single-Layer Graphene. *Phys. Rev. Lett.* **2012**, 108 , 196102.
- (22) Susi, T.; Meyer, J. C.; Kotakoski, J. Quantifying Transmission Electron Microscopy Irradiation Effects Using Two-Dimensional Materials. *Nat Rev Phys.* **2019**, 1, 397–405.
- (23) Cho, H.; Jones, M. R.; Nguyen, S. C.; Hauwiller, M. R.; Zettl, A.; Alivisatos, A. P. The Use of Graphene and Its Derivatives for Liquid-Phase Transmission Electron Microscopy of Radiation-Sensitive Specimens. *Nano Letters.* **2017**, 17, 414–420.
- (24) Rothmann, M. U.; Li, W.; Zhu, Y.; Bach, U.; Spiccia, L.; Etheridge, J.; Cheng, Y.-B. Direct Observation of Intrinsic Twin Domains in Tetragonal CH<sub>3</sub>NH<sub>3</sub>PbI<sub>3</sub>. *Nat Commun.* **2017**, 8, 14547.
- (25) Zhang, D.; Zhu, Y.; Liu, L.; Ying, X.; Hsiung, C.-E.; Sougrat, R.; Li, K.; Han, Y. Atomic-Resolution Transmission Electron Microscopy of Electron Beam–Sensitive Crystalline Materials. *Science.* **2018**, 359, 675–679.
- (26) Rothmann, M. U.; Kim, J. S.; Borchert, J.; Lohmann, K. B.; O’Leary, C. M.; Shearer, A. A.; Clark, L.; Snaith, H. J.; Johnston, M. B.; Nellist, P. D.; Herz, L. M. Atomic-Scale Microstructure of Metal Halide Perovskite. *Science.* **2020**, 370, eabb5940.

- (27) Haider, M.; Uhlemann, S.; Schwan, E.; Rose, H.; Kabius, B.; Urban, K. Electron microscopy image enhanced. *Nature*. **1998**, *392*, 768–769.
- (28) Bosman, M.; Keast, V. J.; García-Muñoz, J. L.; D'Alfonso, A. J.; Findlay, S. D.; Allen, L. J. Two-Dimensional Mapping of Chemical Information at Atomic Resolution. *Phys. Rev. Lett.* **2007**, *99*, 086102.
- (29) Bell, D.; Zandbergen, H. A JEOL-Based Cooling Holder with a Low Specimen Drift Allowing Sub 1 Å STEM Imaging. In *European Microscopy Congress 2016: Proceedings (Ed.)*, **2016**, 352–353.
- (30) E. Tyukalova, R. Satish, R. Chua Yong Sheng, M. Srinivasan, M. Duchamp Structural Evolution of  $\text{LiNi}_{0.5}\text{Mn}_{1.5}\text{O}_4$  Cathode Material by Low Temperature (S)TEM. *10th International Conference on Materials for Advanced Technologies (ICMAT)*, Marina Bay Sands, Singapore, 23-28 June 2019.
- (31) Goodge, B. H.; Bianco, E.; Schnitze, N.; Zandbergen, H. W.; Kourkoutis, L. F. *Microscopy and Microanalysis* **2019**, *25* (S2), 930-931.
- (32) Dubochet, J. On the Development of Electron Cryo-Microscopy (Nobel Lecture). *Angew. Chem. Int. Ed.* **2018**, *57*, 10842–10846.
- (33) Le Ferrand, H.; Duchamp, M.; Gabryelczyk, B.; Cai, H.; Miserez, A. Time-Resolved Observations of Liquid–Liquid Phase Separation at the Nanoscale Using in Situ Liquid Transmission Electron Microscopy. *J. Am. Chem. Soc.* **2019**, *141*, 7202–7210.
- (34) Twitchett, A. C.; Dunin-Borkowski, R. E.; Hallifax, R. J.; Broom, R. F.; Midgley, P. A. Off-Axis Electron Holography of Unbiased and Reverse-Biased Focused Ion Beam Milled Si p-n Junctions. *Microsc Microanal.* **2005**, *11*, 66–78.
- (35) Han, M.-G.; Smith, D. J.; McCartney, M. R. In Situ Electron Holographic Analysis of Biased Si  $n^+$ -p Junctions *Appl. Phys. Lett.* **2008**, *92*, 143502.
- (36) Cavalca, F.; Laursen, A. B.; Kardynal, B. E.; Dunin-Borkowski, R. E.; Dahl, S.; Wagner, J. B.; Hansen, T. W. In Situ Transmission Electron Microscopy of Light-Induced Photocatalytic Reactions. *Nanotechnology*. **2012**, *23*, 075705.
- (37) Wolf, D.; Lubk, A.; Lenk, A.; Sturm, S.; Lichte, H. Tomographic Investigation of Fermi Level Pinning at Focused Ion Beam Milled Semiconductor Surfaces. *Appl. Phys. Lett.* **2013**, *103*, 264104.
- (38) M. Duchamp, V. Migunov, A. Tavabi, A. Mehomic, M. Munde, A.J. Kenyon and R.E. Dunin-Borkowski Advances in in-situ TEM characterization of silicon oxide resistive switching memories Resolution and Discovery **2016**, *1*, 27-33.
- (39) Ishioka, J.; Kogure, K.; Ofuji, K.; Kawaguchi, K.; Jeem, M.; Kato, T.; Shibayama, T.; Watanabe, S. In Situ Direct Observation of Photocorrosion in ZnO Crystals in Ionic Liquid Using a Laser-Equipped High-Voltage Electron Microscope. *AIP Advances*. **2017**, *7*, 035220.
- (40) Ignatans, R.; Damjanovic, D.; Tileli, V. Local Hard and Soft Pinning of  $180^\circ$  Domain Walls in  $\text{BaTiO}_3$  Probed by in Situ Transmission Electron Microscopy. *Phys. Rev. Materials*. **2020**, *4*, 104403.

- (41) Ignatans, R.; Damjanovic, D.; Tileli, V. Individual Barkhausen Pulses of Ferroelastic Nanodomains. ArXiv:2011.05842
- (42) Jones, L.; Yang, H.; Pennycook, T. J.; Marshall, M. S. J.; Van Aert, S.; Browning, N. D.; Castell, M. R.; Nellist P. D. Smart Align—a new tool for robust non-rigid registration of scanning microscope data *Advanced Structural and Chemical Imaging* **2015**, 1, 1-16.
- (43) Savitzky, B. H.; El Baggari, I.; Clement, C. B.; Waite, E.; Goodge, B. H.; Baek, D. J.; Sheckelton, J. P.; Pasco, C.; Nair, H.; Schreiber, N. J.; Hoffman, J.; Admasu, A. S.; Kim, J.; Cheong, S.-W.; Bhattacharya, A.; Schlom, D. G.; Mc Queen, T. M.; Hovden, R.; Kourkoutis L. F. Image registration of low signal-to-noise cryo-STEM data *Ultramicroscopy* **2018**, 191, 56.
- (44) van Huis, M. A.; Young, N. P.; Pandraud, G.; Creemer, J. F.; Vanmaekelbergh, D.; Kirkland, A. I.; Zandbergen, H. W. Atomic Imaging of Phase Transitions and Morphology Transformations in Nanocrystals. *Adv. Mater.* **2009**, 21, 4992–4995.
- (45) Allard, L. F.; Bigelow, W. C.; Jose-Yacaman, M.; Nackashi, D. P.; Damiano, J.; Mick, S. E. A New MEMS-Based System for Ultra-High-Resolution Imaging at Elevated Temperatures. *Microsc. Res. Tech.* **2009**, 72, 208–215.
- (46) Schaffer, M.; Schaffer, B.; Ramasse, Q. Sample Preparation for Atomic-Resolution STEM at Low Voltages by FIB. *Ultramicroscopy*. **2012**, 114, 62–71.
- (47) Giannuzzi, L. A.; Drown, J. L.; Brown, S. R.; Irwin, R. B.; Stevie, F. A. Focused Ion Beam Milling and Micromanipulation Lift-Out for Site Specific Cross-Section Tem Specimen Preparation. *MRS Proc.* **1997**, 480, 19.
- (48) Langford, R. M.; Petford-Long, A. K. Preparation of Transmission Electron Microscopy Cross-Section Specimens Using Focused Ion Beam Milling. *Journal of Vacuum Science & Technology A: Vacuum, Surfaces, and Films.* **2001**, 19, 2186–2193.
- (49) Duncan, H.; Hai, B.; Leskes, M.; Grey, C. P.; Chen, G. Relationships between Mn 3+ Content, Structural Ordering, Phase Transformation, and Kinetic Properties in  $\text{LiNi}_x\text{Mn}_{2-x}\text{O}_4$  Cathode Materials. *Chemistry of Materials.* **2014**, 26, 5374–5382.
- (50) Qiao, R.; Wray, L. A.; Kim, J.-H.; Pieczonka, N. P. W.; Harris, S. J.; Yang, W. Direct Experimental Probe of the Ni(II)/Ni(III)/Ni(IV) Redox Evolution in  $\text{LiNi}_{0.5}\text{Mn}_{1.5}\text{O}_4$  Electrodes. *The Journal of Physical Chemistry C.* **2015**, 119, 27228–27233.
- (51) Arai, H.; Sato, K.; Orikasa, Y.; Murayama, H.; Takahashi, I.; Koyama, Y.; Uchimoto, Y.; Ogumi, Z. Phase Transition Kinetics of  $\text{LiNi}_{0.5}\text{Mn}_{1.5}\text{O}_4$  Electrodes Studied by in Situ X-Ray Absorption near-Edge Structure and X-Ray Diffraction Analysis. *J. Mater. Chem. A.* **2013**, 1, 10442.
- (52) Gao, P.; Ishikawa, R.; Tochigi, E.; Kumamoto, A.; Shibata, N.; Ikuhara, Y. Atomic-Scale Tracking of a Phase Transition from Spinel to Rocksalt in Lithium Manganese Oxide. *Chem. Mater.* **2017**, 29, 1006–1013.
- (53) [Barthel, J. Dr. Probe: A software for high-resolution STEM image simulation. \*Ultramicroscopy\* \*\*2018\*\*, 193, 1-11.](#)

(54) ~~F.~~ Jona ~~F.~~ and ~~G.~~ Shirane ~~G.~~, *Ferroelectric Crystals* (Dover Publications, 1993) <https://doi.org/10.1002/zamm.19630431016>].

(54) Abelmann, L. Magnetic Force Microscopy. In *Encyclopedia of Spectroscopy and Spectrometry (Second Edition)*; John C. Lindon. Academic Press, 2010, 1415-1425.

(55) Montazeri, M.; Upadhyaya, P.; Onbasli, M. C.; Yu, G.; Wong, K. L.; Lang, M.; Fan, Y.; Li, X.; Khalili Amiri, P.; Schwartz, R. N.; Ross, C. A.; Wang, K. L. Magneto-Optical Investigation of Spin-Orbit Torques in Metallic and Insulating Magnetic Heterostructures. *Nat. Commun.* **2015**, *6*, 8958.

(56) Xia, W. X.; Chun, Y. S.; Aizawa, S.; Yanagisawa, K.; Krishnan, Kannan. M.; Shindo, D.; Tonomura, A. Investigation of Magnetic Structure and Magnetization Process of Yttrium Iron Garnet Film by Lorentz Microscopy and Electron Holography. *Journal of Applied Physics.* **2010**, *108*, 123919.

(57) Soumah, L.; Beaulieu, N.; Qassym, L.; Carrétéro, C.; Jacquet, E.; Lebourgeois, R.; Ben Youssef, J.; Bortolotti, P.; Cros, V.; Anane, A. Ultra-Low Damping Insulating Magnetic Thin Films Get Perpendicular. *Nat. Commun.* **2018**, *9* (1), 3355.

(58) Medwal, R.; Chaudhuri, U.; Vas, J. V.; Deka, A.; Gupta, S.; Duchamp, M.; Asada, H.; Fukuma, Y.; Mahendiran, R.; Rawat, R. S. Magnetoimpedance of Epitaxial  $\text{Y}_3\text{Fe}_5\text{O}_{12}$  (001) Thin Film in Low-Frequency Regime. *ACS Appl. Mater. Interfaces.* **2020**, *12*, 41802–41809.

(59) Baños-López, E.; Sánchez-De Jesús, F.; Cortés-Escobedo, C.; Barba-Pingarrón, A.; Bolarín-Miró, A. Enhancement in Curie Temperature of Yttrium Iron Garnet by Doping with Neodymium. *Materials.* **2018**, *11*, 1652.

(60) Shashank, U.; Medwal, R.; Shibata, T.; Nongjai, R.; Vas, J. V.; Duchamp, M.; Asokan, K.; Rawat, R. S.; Asada, H.; Gupta, S.; Fukuma, Y. Enhanced Spin Hall Effect in S-Implanted Pt *Adv. Quantum Technol.* **2021**, *4*, 2000112.

(61) Gupta, S.; Medwal, R.; Kodama, D.; Kondou, K.; Otani, Y. C.; Fukuma, Y. Important role of magnetization precession angle measurement in inverse spin Hall effect induced by spin pumping *Appl. Phys. Lett.* **2017**, *110*, 022404.

(62) Avci, C. O.; Quindeau, A.; Pai, C.-F.; Mann, M.; Caretta, L.; Tang, A. S.; Onbasli, M. C.; Ross, C. A.; Beach G. S. D. Current-induced switching in a magnetic insulator *Nature Materials* **2017**, *16*, 309–314.

(63) Kläui, M.; Vaz, C. A. F.; Bland, J. A. C.; Wernsdorfer, W.; Faini, G.; Cambril, E.; Heyderman, L. J.; Nolting, F.; Rüdiger U. Controlled and reproducible domain wall displacement by current pulses injected into ferromagnetic ring structures *Phys. Rev. Lett.* **2005**, *94*, 106601.

(64) Parkin, S. S. P.; Hayashi, M.; Thomas, L. Magnetic domain-wall racetrack memory *Science* **2008**, *320*, 190–194.

(65) Tatara, G.; Kohno, H. Theory of current-driven domain wall motion: spin transfer versus momentum transfer. *Phys. Rev. Lett.* **2004**, *92*, 086601.